

Realizing the heteromorphic superlattice: Repeated heterolayers of amorphous insulator and polycrystalline semiconductor with minimal interface defects

Woongkyu Lee¹, Xianyu Chen¹, Qing Shao², Sung-Il Baik¹, Sungkyu Kim¹, David Seidman¹, Michael Bedzyk^{1,3}, Vinayak Dravid¹, John B. Ketterson³, Julia Medvedeva^{4*} (https://orcid.org/0000-0001-7142-1644), Robert P. H. Chang^{1*}, Matthew A. Grayson^{2*} (https://orcid.org/0000-0003-4914-5043)

¹Department of Materials Science and Engineering, Northwestern University, Evanston, Illinois 60208, US

²Department of Electrical Engineering and Computer Science, Northwestern University, Evanston, Illinois 60208, US

³Department of Physics and Astronomy, Northwestern University, Evanston, Illinois 60208, US

⁴Department of Physics, Missouri Science and Technology University, Rolla, Missouri 65409, US.

*m-grayson@northwestern.edu, r-chang@northwestern.edu, juliaem@mst.edu

Abstract

An unconventional "heteromorphic" superlattice (HSL) is realized, comprised of repeated layers of different materials with differing morphologies: semiconducting pc-In₂O₃ layers interleaved with insulating a-MoO₃ layers. Originally proposed by Tsu in 1989, yet never fully realized, the high quality of the HSL heterostructure demonstrated here validates the intuition of Tsu, whereby the flexibility of the bond angle in the amorphous phase and the passivation effect of the oxide at interfacial bonds serve to create smooth, high-mobility interfaces. The alternating amorphous layers prevent strain accumulation in the polycrystalline layers while suppressing defect propagation across the HSL. For the HSL with

THIS ARTICLE HAS BEEN ACCEPTED FOR PUBLICATION AND UNDERGONE FULL PEER REVIEW BUT HAS NOT BEEN THROUGH THE COPYEDITING, TYPESETTING, PAGINATION AND PROOFREADING PROCESS, WHICH MAY LEAD TO DIFFERENCES BETWEEN THIS VERSION AND THE <u>VERSION OF RECORD</u>. PLEASE CITE THIS ARTICLE AS <u>DOI: 10.1002/ADMA.202207927</u>.

THIS ARTICLE IS PROTECTED BY COPYRIGHT. ALL RIGHTS RESERVED.

7:7 nm layer thickness, the observed electron mobility of 71 cm 2 /Vs, matches that of the highest quality In $_2$ O $_3$ thin films. The atomic structure and electronic properties of crystalline In $_2$ O $_3$ / amorphous MoO $_3$ interfaces are verified using *ab-initio* molecular dynamics simulations and hybrid functional calculations. This work generalizes the superlattice concept to an entirely new paradigm of morphological combinations.

1. Introduction

The original introduction of heteroepitaxial superlattices with crystalline morphology by Leo Esaki and Raphael Tsu in 1970^[1] laid the foundation for many modern materials breakthroughs such as the enhancement of electron mobility with modulation doping, [2] the observation of Bloch oscillations, [3] the invention of quantum cascade lasers, [4] and more recently, polar interfaces in oxide heterostructures which lead to emergent order for spin, charge, and orbital degrees of freedom^[5] including superconductivity.^[6] Lesser known is a follow-up proposal by Raphael Tsu in 1989^[7] to further generalize the superlattice concept by growing repeated layers of different materials with different morphologies - one polycrystalline (pc), one amorphous (a) – thereby bestowing the functional advantages of superlattices to an even broader class of materials combinations. Here the name "heteromorphic superlattice" (HSL) is used to designate different material layers with different morphologies, in contrast with the term polymorphic^[8] which refers to the same stoichiometric material in different phases. With heuristic arguments, Tsu proposed that the interface chemistry of the amorphous component would allow both greater freedom of bond angles at the interface to reduce strain and greater bond passivation of the polycrystalline component to eliminate dangling bonds, thereby leading to reduced defect density and high electron mobility with "grain boundaries effectively passivated by amorphous materials."[1] However, the original attempts to realize even a single period of this structure with the polycrystalline / amorphous paring of pc-Si/a-SiO2 yielded only semiconducting quantum dots embedded within a single oxide layer, [9] and subsequent attempts yielded only highly insulating structures, [10,11,12] leaving Tsu's original prediction of a semiconducting SL unsatisfied.

Tsu's proposition was subsequently joined with a large body of work on *single* heterointerfaces between (poly)crystalline and amorphous phases, where a majority focused on passivation of dangling bonds at the interface with extrinsic hydrogen, but only a rare few attempted amorphous/crystalline *multilayers*. Interestingly, *none* of these HSL structures were directly deposited, but instead realized via layer-selective phase transitions. Heterolayer superlattices that were initially grown as purely *crystalline* underwent a layer-selective phase transition to amorphous via electrical or optical

excitation or thermal annealing,^[14] via irradiation by high-energy ion beams,^[15] or via selective etching.^[16] Or heterolayers initially grown as purely *amorphous* underwent layer-selective phase transition to crystalline via thermal annealing.^[17,18,19] One particularly creative approach rolled up a single amorphous/crystalline heterolayer on a sacrificial strain layer to achieve a radial superlattice.^[20] However, as mentioned previously, none of these structures were *as-grown* mixed-morphology HSLs, and none of these works tested Tsu's original proposal that the bond-angle flexibility at the intrinsic amorphous interface could serve to passivate dangling bonds.

The present paper uses precision sub-monolayer pulsed laser deposition (PLD) to demonstrate the successful fabrication of a Tsu HSL by choosing oxide compounds for each layer which have different morphologies under the same growth conditions: the polycrystalline semiconducting oxide pc-In₂O₃ as the "well" layer and the amorphous insulating oxide α -MoO₃ as the "barrier" layer. The pc-In₂O₃ is chosen as a representative high-mobility oxide to give electrical sensitivity to the interface quality, and the a-MoO₃ is chosen since its crystalline form would already permit strain relief via sliding of 2D Van der Waals layers, [21,22,23] and its amorphous form might be expected just as compliant. And whereas standard heteroepitaxy that maintains lattice periodicity can accumulate straininduced defects with increasing SL periods, [24,25,26,27,28,29] the HSL structure would inherently relax strain within each period, with polycrystalline layers thinner than the critical thickness for defect formation interrupted by strain-relieving alternate amorphous layers. [3] The high quality of the interfaces is demonstrated with electron microscopy and X-ray spectroscopy, and high electron mobility is verified in electrical transport. To bolster the intuition in Tsu's original paper, [1] ab-initio molecular dynamics and hybrid functional calculations are performed to model the interface between crystalline In₂O₃ and amorphous MoO₃. These studies corroborate Tsu's original intuition that the relaxation of the bond angles and passivation of dangling bonds at the interface result in reduced defect density and, in turn, contribute to the experimentally observed high electron mobilities.

2. Experimental and computational methods

In this section, the experimental process, procedures, related equipment and the calculation details are described.

2.1 Thin film growth by PLD

Accepte

We emphasize that both pc-In₂O₃ and a-MoO₃ films are grown under identical growth conditions including identical growth temperature and identical ambient oxygen pressure. Oxide thin films are deposited by PLD with a 248 nm KrF excimer laser. The laser pulse duration is 25 ns and the pulse frequency is 2 Hz. Each pulse of 220 mJ is focused to 1 mm \times 3 mm area at the target, which rotates at 5 rpm. pc-In₂O₃ and a-MoO₃ thin films are deposited from hot-pressed In₂O₃ and MoO₃ targets (25 mm diameter), respectively. Fused quartz substrates are mounted to the substrate holder with silver paste. The distance between the target and substrate is fixed to 10 cm. The chamber is pumped out before each deposition by the turbomolecular pump until the pressure reaches under 5 \times 10⁻⁷ Torr. The flow of high-purity O₂ to the chamber is precisely controlled during deposition to obtain target oxygen pressure, and the temperature of the substrate is controlled by the electric resistive heated substrate holder. The optimal deposition pressure and temperature are 15 mTorr and 200 °C, respectively. Figure S1 in supporting information (SI) shows the schematic diagram of the PLD system.

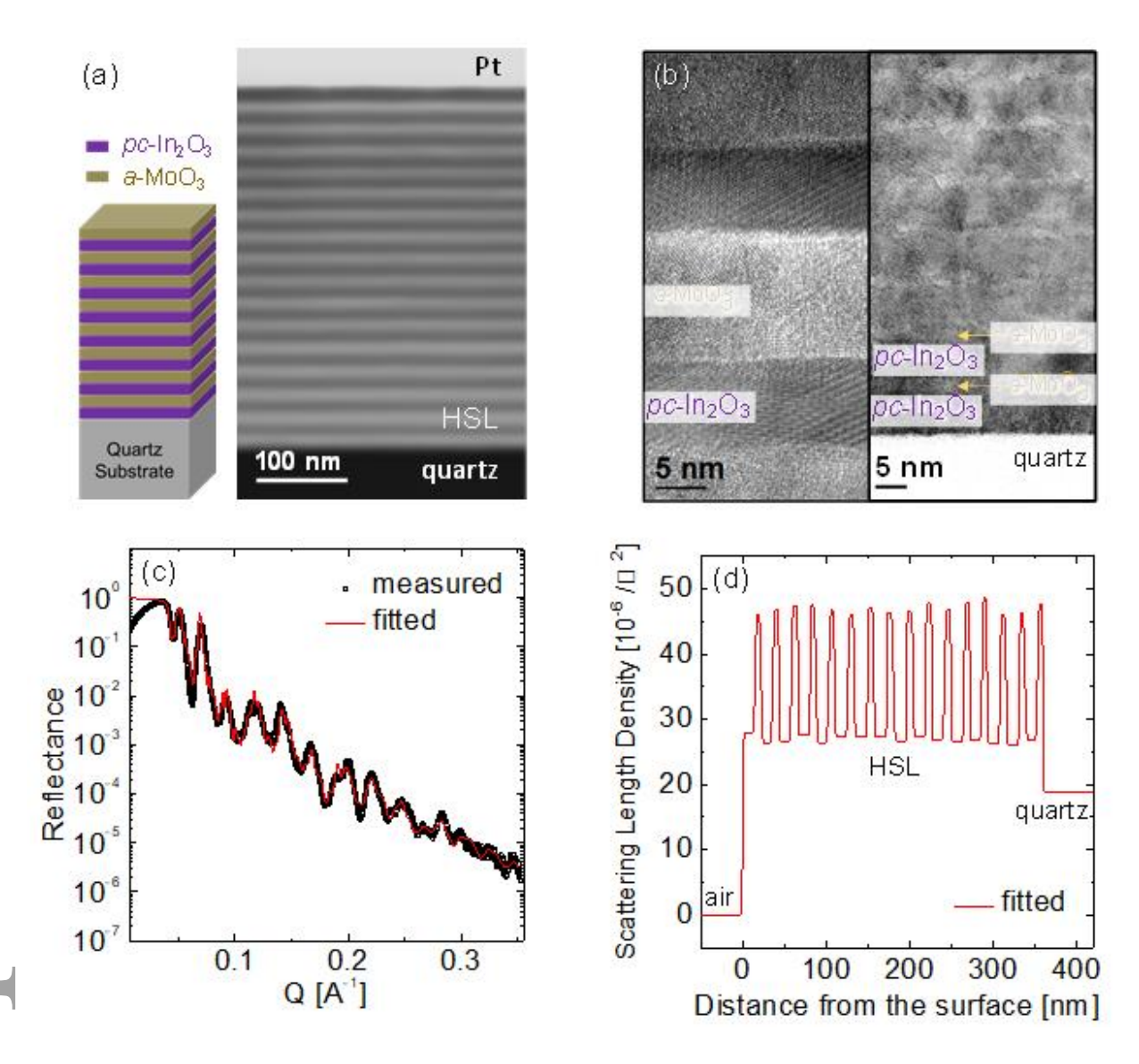


Figure 1. Physical structure of the HSL films. (a) Cross-sectional scanning TEM image of a 16-bilayer HSL (7 nm pc-In₂O₃ / 15 nm a-MoO₃) on a quartz substrate. Inset: HSL schematic. (b) Bright-field high-resolution TEM image of the equivalent sample (left panel) and image of a 16-bilayer HSL (7 nm pc-In₂O₃ / 0.5 nm a-MoO₃) (right panel). The Pt capping layer is adopted to protect the sample. (c) XRR data and the fitted model showing remarkable agreement in the fine structure of HSL. (d) The scattering length density profile is obtained from the XRR fitting of the data in (c).

2.2 Characterization

Thin films are characterized using transmission electron microscopy (TEM, JEOL, JEM-2100F / JEM-ARM 300F) to investigate the cross-sectional morphology of the films, including

15214095, ja, Downloaded from https://onlinelibrary.wiley.com/doi/10.1002/adma.202207927 by Readcube (Labtiva Inc.), Wiley Online Library on [260342023]. See the Terms and Conditions (https://onlinelibrary.wiley.com/terms-and-conditions) on Wiley Online Library for rules of use; OA articles are governed by the applicable Creative Commons

thickness, crystal structure, and interface quality. TEM samples are prepared using a standard technique employing a focused ion beam (FIB, FEI, Helios Nanolab 600 dual-beam) microscope with Ga+ energy of 2 keV at 24 pA ion current. The surface morphology and cross-section images of oxide films are analyzed by field emission scanning electron microscopy (FESEM, Hitachi, SU8030). The surface morphology and the root-mean-squared roughness are obtained by atomic force microscopy (AFM, Bruker, Dimension FastScan). The thickness of the films is measured by spectral reflectometer (Filmetrics, F20) and reconfirmed by stylus profilometer (Veeco, Dektak 150) and X-ray reflectivity (XRR) using Cu K α X-ray source (Rigaku, Smartlab). The crystal structure of the film is analyzed by X-ray diffraction (XRD), and the thickness, density, and roughness are investigated by XRR. A 100 nm thick pc-In₂O₃ layer and a pc-MoO₃ layer are deposited by PLD on separate quartz substrates to confirm the growth rate. Their measured thicknesses are consistent as measured with a stylus profilometer, XRR, and spectral reflectometer as shown in Figure S2. Carrier density, mobility, and resistivity of the oxide films at room temperature are obtained via the Van der Pauw method with a Hall effect measurement system (Ecopia, HMS-3000).

2.3. Calculations

Simulations of α -MoO₃ bulk structures are obtained using ab-initio molecular dynamics (MD) liquid-quench approach as implemented in the Vienna Ab Initio Simulation Package (VASP). The calculations are based on density functional theory (DFT) with periodic boundary conditions and employ the Perdew-Burke-Ernzerhof (PBE) functional within the projector augmented-wave method. For the simulation of the HSL interface, alternating layers of 68-atom amorphous MoO₃ and an 80-atom [100]-oriented crystalline In_2O_3 are constructed with periodic boundary conditions, creating two interfaces in one global crystallographic direction with infinite oxide planes along the other two directions. Five structures for α -MoO₃ bulk with the optimal density are employed for the simulation, resulting in five independent a-MoO₃/c-In₂O₃ interfacial models. The details of the theoretical approach method are described in SI.

3. Results and discussion

HSL fabrication

The alternating heteromorphic units of polycrystalline-semiconducting and amorphous-insulating layers are seen in the left-side schematic of Figure 1(a). The material choices for HSLs can, in principle, range from semiconductors to magnetic materials and superconductors. As an example, the present study employs polycrystalline semiconducting In_2O_3 and amorphous insulating MoO_3 grown via PLD (Figure S1), whereby the layer

thicknesses of the HSL structures can be controlled to sub-monolayer precision. These materials are chosen since alternate layers of highly crystalline In_2O_3 and amorphous MoO_3 can both be deposited with highly reproducible properties at identical growth temperatures and oxygen partial pressures of $T_g = 200$ °C and $P_{O2} = 15$ mTorr, to assure full oxidation and minimum defects, with all other deposition parameters fixed. With the crystallization temperature of In_2O_3 at $I_1 = 25$ °C for crystalline fraction >80% for 350 nm films, $I_2 = 300$ °C, the growth temperature $I_3 = 300$

pc-In₂O₃ / a-MoO₃ interface characterization in HSL

Maintaining a sharp growth interface throughout the whole HSL up to the final deposition layer is crucial for proper realization of an HSL. To evaluate the interface quality of the fabricated HSL, high-resolution cross-sectional TEM, scanning TEM, XRD, XRR, and AFM analyses are carried out. Note that the total layer thickness of the diagnostic structures considered here (circa 350 nm) may be thicker than necessary for typical devices, but the purpose here is to demonstrate the ability to achieve smooth multilayers even in excess of standard thicknesses.

Figure 1(a) shows a layer schematic of HSL and a scanning TEM image of a 16-period HSL consisting of 7 nm pc-In₂O₃ / 15 nm a-MoO₃, where the brighter lines correspond to the In₂O₃ layer. Note the layers remain parallel throughout the structure with sharp boundaries. The left side of Fig. 1(b) shows the higher-magnification bright-field TEM image of an equivalent HSL. The sharp interfaces between pc-In₂O₃ and a-MoO₃, have roughness much less than a nanometer. The right side of Figure 1(b) demonstrates growth of α-MoO₃ layers as thin as 0.5 nm between In₂O₃ polycrystalline layers. The sharpness of the pc-In₂O₃ / a-MoO₃ interface can also be observed from the X-ray reflectance of Fig. 1(c), which shows the XRR of a HSL sample with the same structure as in Figure 1(a). Despite the complex structure of the HSL and the large number of layers, the XRR data can be fitted with a highprecision model using MOTOFIT software, [31] as depicted by the red line in the same graph. This fit is able to yield the average thickness of each layer, as well as the average X-ray scattering length density, from which the mass density of each layer can be calculated [32,33] with knowledge of the ideal bulk scattering length density values of In₂O₃ and MoO₃. [34] The results for the In₂O₃ layers (with ± indicating standard deviation) are an average thickness of 7.2 \pm 0.5 nm, average scattering length density of $47.0 \times 10^{-6} \pm 0.8 \times 10^{-6}$ Å⁻²), and density of 6.28 ± 0.11 g/cm³. For a-MoO₃, the average layer thickness is 15.3 ± 0.6 nm, the average scattering length density is $26.8 \times 10^{-6} \pm 0.5 \times 10^{-6} \text{ Å}^{-2}$, and the mass density is 3.43 ± 0.06

5214095, ja, Downloaded from https://onlinelibrary.wiley.com/doi/10.1002/adma.202207927 by Readcube (Labtiva Inc.), Wiley Online Library on [26/03/2023]. See the Terms and Conditions (https://onlinelibrary.wiley.com/kems-and-conditions) on Wiley Online Library for rules of use; OA articles are governed by the applicable Creative Commons

g/cm³. From these results, the In_2O_3 and MoO_3 layers have mass density ratios of 87.5% and 73.2% relative to the ideal bulk values (In_2O_3 : 7.18g/cm³, MoO_3 : 4.69 g/cm³). In_3O_3 and In_3O_3 relative to the ideal bulk values (In_2O_3 : 7.18g/cm³, In_3O_3 : 4.69 g/cm³). In_3O_3 and interfaces is about 0.9 nm, which is consistent with that seen in Fig. 1(b). The variations of scattering density, roughness, and thickness of each layer from the surface down to the substrate obtained by the simulation of Fig. 1(c) are depicted in Figure 1(d). The raw values of the fit for Fig. 1(d) are shown in Table S1 in the SI. The scattering length density and thickness of the same material layers are thus very uniform, and the interfaces between layers are sharp and distinct. The growth rates of In_2O_3 and In_2O_3 and In

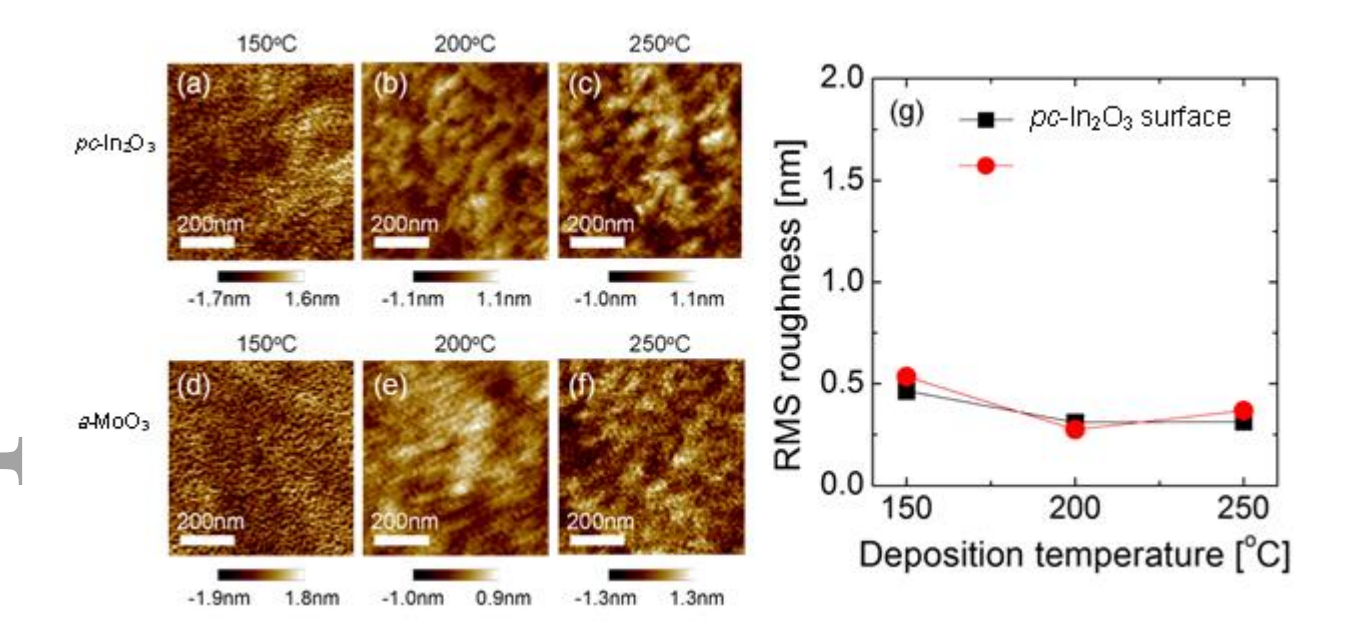


Figure 2. Surface morphology of pc-In₂O₃ and a-MoO₃ layers. The AFM topographic images of the top 7 nm pc-In₂O₃ layer of 16 bilayers (7 nm pc-In₂O₃ / 15 nm a-MoO₃) deposited at (a) 150 °C, (b) 200 °C, and (c) 250 °C, respectively. The AFM topographic images of the top a-MoO₃ layer similarly atop 16 bilayers grown at (d) 150 °C, (e) 200 °C, and (f) 250 °C, respectively. (g) The summary of the RMS surface roughness obtained from (a-f) implies extremely sharp interfaces throughout.

The AFM images in Fig. 2 indicate the film surface roughness of pc-In₂O₃ and a-MoO₃, respectively, as a function of deposition temperature, and verify the atomically smooth

surface at the growth temperature of 150-250 °C. The minimal surface roughness of both the topmost pc-In₂O₃ layers in Fig. 2(a-c) and, alternately, the topmost a-MoO₃ layers in Fig. 2(d-f) of the HSL sample despite the overall SL thickness of 350 nm verifies the sharpness of the interfaces observed in Figure 1.

Crystalline versus amorphous order of In₂O₃ and MoO₃ layers, respectively

To verify the HSL morphology, the crystalline or amorphous nature of the respective layers must be carefully examined and validated. ^[1] Thus the selective area diffraction patterns (SADPs) from TEM and high-resolution XRD analyses are examined.

Figure 3(a) shows the SADPs obtained from the sample. The magnification is controlled so that the whole multilayer oxide region is sampled in the SADP image. The diffraction spots marked by the purple arrows 'a' and 'b', indicate In_2O_3 features which match well with the (222) and (211) planes, respectively, of the cubic (bixbyite, space group of Ia-3) structure of In_2O_3 . (Ref: ICDD 00-006-0416) It is noted that many diffraction patterns, especially the 'a' spots, are positioned at the top side of the transmitted electron beam. This implies that the sample has strong (222)-texture in the multilayer growth direction. This corroborates the XRD results in Figure 3(b) which also shows high preferred orientation of the (222) plane. The amorphous ring indicated by the gold arrow 'c' indicates lack of long-range order in the pure amorphous MoO_3 layer grown at these temperatures.

Figure 3(b) shows the theta-2 theta XRD patterns of a 280-nm-thick In_2O_3 single layer, a 7 nm pc- In_2O_3 / 15 nm a-MoO $_3$ HSL consisting of ×16 bilayers (with a total thickness of 352 nm), a 400-nm-thick MoO $_3$ single layer on a fused quartz substrate, and finally a fused quartz substrate with no deposition. The broad feature around 22° is seen to result from the fused quartz substrate, alone. In the single layer In_2O_3 (purple), a very sharp and intense peak from the (222) plane appears at around 30.1° as well as peaks from the (211), (400), (332), (431), (440), (622), and (444) planes, with calibrated crystalline planes from ICDD 00-006-0416 marked with vertical lines. Although the HSL had high (222)-preferred orientation, the Laue oscillations were hard to observe due to the small nonunifomity of repeated bilayers in the HSL. From the SEM image (Fig. S3), the thick In_2O_3 is observed to grow in a continuous columnar mode with circa 20 nm diameter columns. Compared to the reference In_2O_3 peak positions shown as vertical gray lines in Figure 3 (b), every peak of the 280-nm-thick In_2O_3 is shifted to the lower angle, indicating residual compressive in-plane strain. However, the XRD peak positions of the HSL sample are better aligned with the *unstrained* bulk In_2O_3 reference peak positions, indicating that no residual strain is present

in the HSL. This suggests the critical role of the alternating layers of crystalline and amorphous films in relieving strain in the polycrystalline layer.

Finally, the slightly enhanced linewidth in Fig. 3(b) of the In_2O_3 peaks in the HSL structure (red) compared to the columnar crystalline layer (purple) indicates greater inhomogeneity of the In_2O_3 layer within the HSL. Since higher-order peaks are not sufficiently resolved, a Williamson-Hall^[38] type analysis cannot distinguish the source of the inhomogeneity, but it can put an upper limit on any possible strain inhomogeneity and a lower limit on typical crystal grain size. The result is a maximum strain inhomogeneity of $\Delta\epsilon=0.006$ for the In_2O_3 single layer and 0.016 for the In_2O_3 layer in the HSL, or, alternatively, a minimum limit of $\delta x=22.22$ nm average crystallite size for the In_2O_3 single layer and 8.2 nm for the In_2O_3 layer in the HSL. We note that the 22.2 nm limit for In_2O_3 is consistent with the approximate horizontal grain size seen in Fig. S3. Since the In_2O_3 single layer was grown in columnar mode, the vertical grain size, corresponding to the extracted crystallite size by XRD, was expected to be similar to or larger than the horizontal grain size. The calculated 8.2 nm crystallite size is consistent with the HSL In_2O_3 layer thickness of 7 nm, thus, the crystal grain size, alone, seems to account for the diffraction peak broadening, aside from any consideration of strain.

HSL enhancement of electron mobility

Accepte

Mobility and electron density are two sensitive indicators of defects as they are both affected by interface charge traps and dangling bonds, while mobility also provides a measure of polycrystalline grain boundary scattering. Thus, the electron transport properties of the semiconducting pc-In₂O₃ layer should be an excellent indicator of growth and interface quality. Following standard methods, mobility for a series of HSL samples is characterized by conducting Hall effect measurements to estimate the free electron density, then measuring the sheet conductance with the Van der Pauw method to deduce the Hall mobility. The total film thickness of circa 350 nm for each sample is confirmed with spectral reflectometry, and the doping is confirmed to be n-type for every sample. For comparison, the 280 nm-thick pure In₂O₃ film from the prior section was measured to establish the baseline mobility and density of pure polycrystalline In₂O₃, namely 7 cm²/Vs. And the 400 nm-thick MoO₃ film from the prior section was confirmed to be highly insulating ($\rho > 10^5$ Ω cm) eliminating the need to consider parallel conduction in these layers.

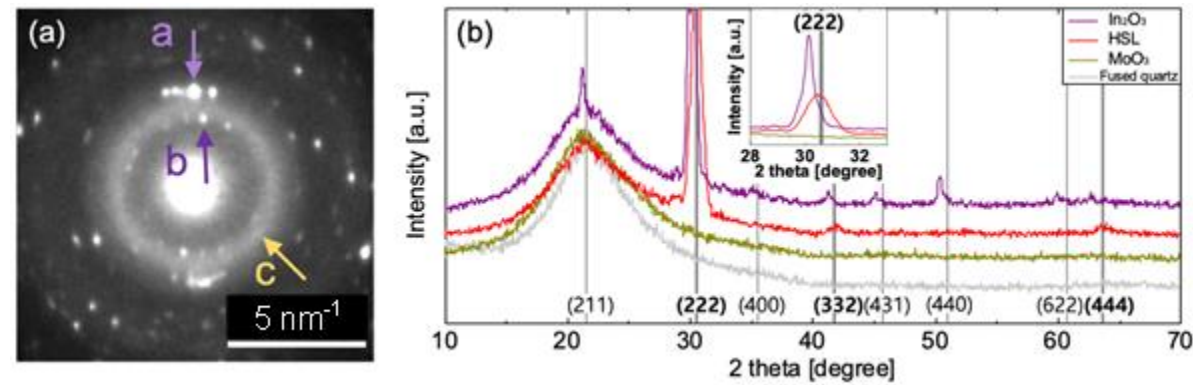


Figure 3. Crystallinity of the HSL films. (a) Selective area diffraction patterns (SADP) of the entire 16-layer 7 nm pc- In_2O_3 / 15 nm a-MoO₃ HSL by TEM. Diffraction spots "a" and "b" for In_2O_3 and the diffraction ring "c" for MoO₃ are described in the text. (b) Theta-2 theta XRD patterns of $280 \text{ nm } In_2O_3$ single layer (purple), 352 nm HSL (red), and $400 \text{ nm } MoO_3$ single layer (gold). The fused quartz substrate (grey) is responsible for the wide amorphous peak at 22° near the (211) line of In_2O_3 . The inset in (b) shows an enlargement in 2-theta range of 28- 33° around the vertical gray lines of In_2O_3 crystalline planes from ICDD 00-006-0416, where a small compressive strain is observed as a left shift of the In_2O_3 polycrystalline layer peak (purple) from the pure bulk crystal (222) plane (vertical grey line), whereas the HSL (red) exhibits no net strain, staying centered around this (222) unstrained diffraction peak. The broadening of the HSL In_2O_3 peak (red) by comparing its full width at half-maximum (FWHM) to the polycrystalline In_2O_3 peak (purple) suggests grain inhomogeneity in the HSL. The lack of any diffraction peaks whatsoever for the pure In_2O_3 layer (gold), by contrast, indicates its amorphous structure at this growth temperature.

The resulting mobilities and carrier densities are shown in Fig. 4. For the samples indicated in purple, the respective layer thicknesses x were kept equal, In_2O_3 :MoO₃ = x:x [nm], revealing in Fig. 4(a) a maximum mobility of 71 cm²/Vs at 7:7 [nm] layer thickness. For the samples indicated in gold, the layer thicknesses maintain the In_2O_3 layer at this optimal value of 7 nm and the MoO₃ layer thickness y was varied In_2O_3 :MoO₃ = 7:y [nm], and again a clear maximum is observed in Fig. 4(a) when both layers are 7 nm thick. Note that all HSL mobilities exceed that of the pure In_2O_3 sample, indicated with the gold arrow at y = 0. The peak electron mobility observed here is consistent with the best mobility in In_2O_3 thin films from prior work. The fact that these layers conduct at all, offers compelling evidence in favor of Tsu's intuition that the HSL is able to effectively passivate the SL interfaces without inducing high densities of dangling bonds that might trap free electron charge density and thereby reduce or eliminate conduction. On top of this, the fact that the mobility in all HSLs is consistently better than that of the bulk pc- In_2O_3 film implies that any density of charge traps at the interface likewise does not contribute significantly to ionized impurity scattering.

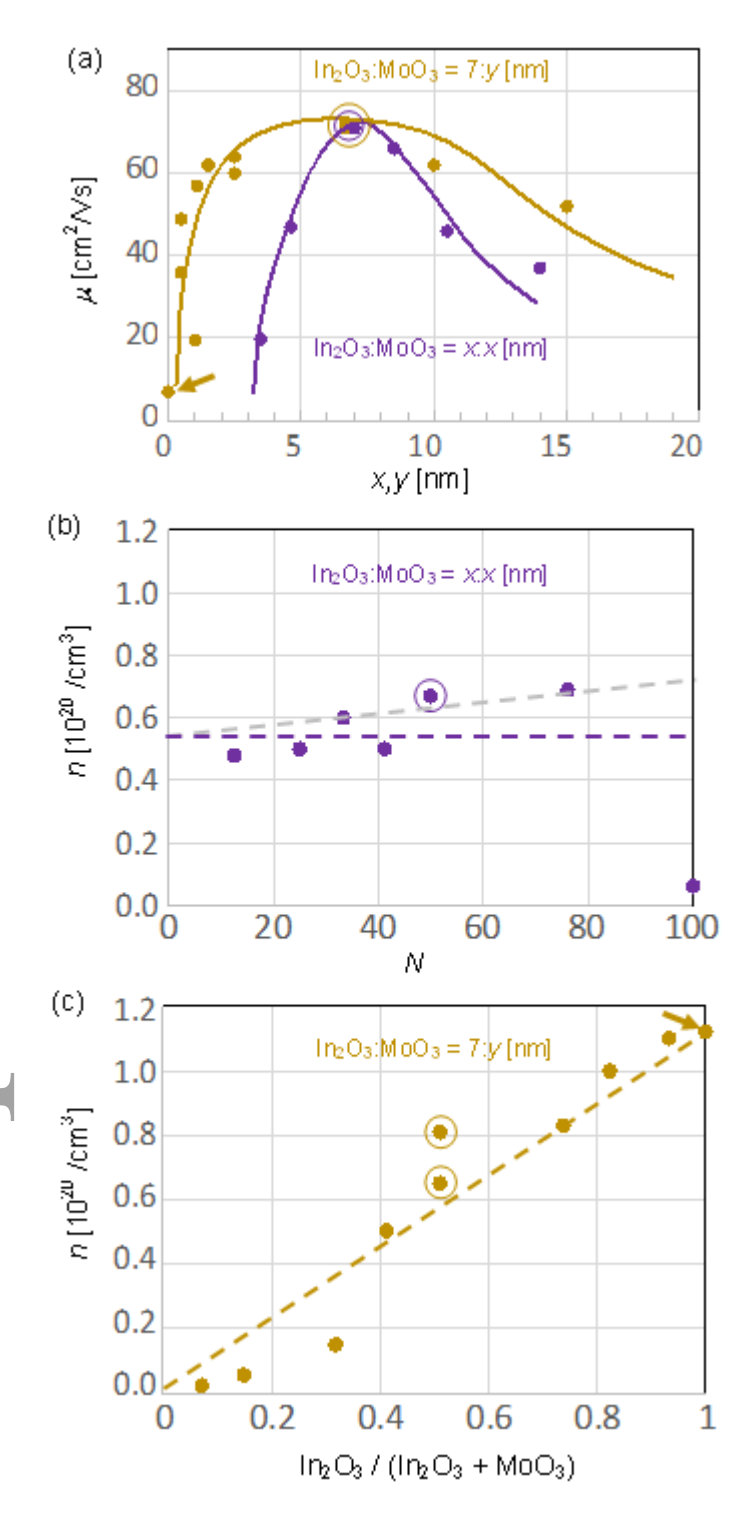


Figure 4. Optimal mobility in HSL films. Various heteromorphic superlattices are grown to find the optimal mobility structure. (a) First, a sequence of SL periods with equal layer thicknesses of $In_2O_3:MoO_3 = x:x$ [nm] (purple filled circles) is grown. Then a $In_2O_3:MoO_3 = 7:y$ [nm] SL sequence is grown where the In_2O_3 layer thickness is held at 7 nm and the MoO_3 layer thickness is varied (gold filled circles). Lines are

guides to the eye. The peak mobility of $\mu = 71 \text{ cm}^2/\text{Vs}$ is observed for both sets of SLs at 7:7 nm (purple and gold open circles) and is about an order of magnitude larger than the pure In_2O_3 polycrystalline layer at x,y=0 (gold arrow). All superlattices have total thickness around 350 nm. (b) The electron density n of the balanced In_2O_3 :MoO₃ = x:x [nm] superlattices is shown relative to the number of SL interfaces N per 350 nm growth. All superlattices have 50% In_2O_3 volume content and therefore about half the average electron density of a pure pc- In_2O_3 layer (horizontal dashed line). Only the extreme case of N=100 interfaces per 350 nm SL at x:x=3.5:3.5 nm deviates strongly from this expected average. The grey dashed line indicates a speculative 2D interface donor density of order $7 \times 10^{12}/\text{cm}^2$ setting an approximate upper bound for the interface donor charge. The open circle indicates the optimal mobility sample in this series. (c) The electron density n of the In_2O_3 :MoO₃ = 7:p [nm] superlattices with varying MoO₃ thickness are shown versus In_2O_3 volume fraction. The approximate agreement with the gold dashed line indicates once again that the electron density is dominated by bulk doping proportional to the In_2O_3 volume fraction. Again, the open circles indicate the optimal mobility samples in this series, and the gold arrow designates the bulk In_2O_3 sample with electron density $1.1 \times 10^{20}/\text{cm}^3$.

Theoretical calculations of crystalline In₂O₃ / amorphous MoO₃ interface

Accepte

To complement experimental evidence of Tsu's heteromorphic interface model, the structural properties of the stoichiometric c- \ln_2O_3/a - MoO_3 interface are investigated using ab-initio MD simulations and accurate hybrid functional calculations. Given the limitations on the size of the simulated supercell, the pc-In₂O₃ is approximated as a single crystalline grain in a unit SL supercell with periodic boundary conditions. In Figure 5(a), the atomic structure of one realization of the stoichiometric c-In₂O₃/ α -MoO₃ model with superlattice layers of approximately 10:10 Å is depicted. Following Tsu, one critical factor for growing HSL structures is the preservation of the stoichiometry. Therefore, in Figure 5(b), the effective coordination numbers of individual In and Mo atoms are calculated, plotted as a function of the z-coordinate of the atom across the interface, and compared to the average value in the stoichiometric c-In₂O₃ bulk and a-MoO₃ bulk, respectively. The results reveal that the majority of Mo atoms within the Mo-O layer (84%) have the effective coordination at or above the bulk value, so that the Mo-O coordination averaged over the total 85 Mo atoms among 5 different interfacial models of the HSL structure is slightly higher (4.0) than the average Mo-O coordination in stoichiometric bulk (3.7). The lowest Mo-O coordination is 3.13, which is still higher than the lowest Mo-O coordination in α -MoO₃ bulk, 3.02. On the contrary, all except one In atom out of 160 total, have the effective coordination at or below that of the c-In₂O₃ bulk value (5.8). It is worthwhile to note that the coordination of 5.0 is

15

slightly above 3.7 and the lowest Mo-O coordination for an individual Mo is 3.06 (Fig. S5). Both values are nearly identical to those in bulk amorphous MoO₃, namely, 3.7 and 3.02, respectively, seen previously in Fig. 5(b). Comparing the band offsets between the molybdenum and indium oxide layers in the stoichiometric and sub-stoichiometric interfaces, the bottom of the conduction band for the crystalline In_2O_3 layer shifts downward with respect to the Mo *d*-states, which corresponds to the doping of the indium oxide layer, as expected from the lower In-O coordination in the sub-stoichiometric interface. Indeed, the calculated charge density distribution within the lowest conduction band reveals the charge localization between two pairs of severely under-coordinated In atoms (Fig. S6.) This supports the interpretation that interfaces induce mild doping per the experimental data of Fig. 4(b), discussed previously.

Comparison to original Tsu superlattice

A word of discussion is in order regarding Tsu's own efforts and those of subsequent groups to create a semiconducting heteromorphic superlattice in the pc-Si/a-SiO₂ system. [2] According to Tsu, an HSL structure should provide high mobility conduction if the dangling bonds at the pc/a interface are passivated, due to both the flexibility of bond angles in the amorphous phase and the presence of oxygen in the oxide for bond passivation. This proved difficult in Tsu's own attempts, where the oxygen from the a-SiO₂ passivation appeared to diffuse through the entire Si layer in some places, resulting in layers of Si quantum dots in a SiO₂ matrix.^[2] And in follow-up studies by other researchers where a layered structure was preserved, the charge traps appear to have rendered the superlattices completely insulating. $^{[21,22,23]}$ In the latter case, this is likely because the bond angles in α -SiO $_2$ were insufficiently flexible to overcome the overly rigid tetragonal bond angles of the pc-Si, resulting in a high density of unpassivated dangling bonds and therefore trapped charge. By contrast, the pc-In₂O₃ investigated here has an amorphous-to-crystalline phase transition near room temperature, so the redirection of bond angles is not energetically expensive, and the pc-ln₂O₃/a-MoO₃ oxide-to-oxide interface has a ready supply of oxygen for passivation of dangling bonds at the interface. The result is a mobility that rivals the best amorphous In₂O₃ layers grown. [16]

4. Conclusion

An unconventional multi-morphology approach is adopted to realize an HSL structure, which sandwiches thin polycrystalline layers of one material between similarly thin amorphous layers of another material. The complementary morphologies in each lattice period appear to greatly suppress interface defects as predicted by Tsu, permitting semiconducting layers

to maintain doping levels consistent with bulk doping. Simultaneously, the interleaved amorphous layers appear to significantly enhance the electron mobility of the polycrystalline layer, suggesting an optimal layer thickness at 7 nm per layer. The low strain observed in XRD and high quality of the charge transport implies that strain and cumulative defects in the polycrystalline In_2O_3 are suppressed with each repeating amorphous layer, and that this defect suppression can continue to an HSL of arbitrary thickness. MD simulations suggest that dangling bonds at the interface are suppressed by the first few layers of atoms in the polycrystalline layer adjacent to the amorphous interface.

By generalizing the superlattice concept beyond purely crystalline morphology, the heteromorphic structure realized here heralds mixed-morphology material combinations that can manifest novel materials properties. We point to challenges in the field of transparent semiconductors which might be met by such HSL structures. For example, increased mobility of transparent semiconductors can enhance switching speed or reduce power consumption in displays, and a modulation-doped HSL with additional doping inside the insulating MoO₃ layer should, in principle, increase the electron mobility for a given electron density, analogous to the originally proposed modulation-doped superlattice of Dingle, et al. [4] Or modulation doped HSLs could compensate for the heavy hole mass in ptype transparent conductors to realize higher mobilities there, as well. Finally, we note that HSLs introduce vertical device functionality such as HSL superlattice minibands or negativedifferential resistance resonant-tunneling-diodes. Preliminary evidence from the authors indicates that phase coherent tunneling across multiple HSL periods can, in fact, be experimentally achieved. [39] This HSL concept should be realizable in other amorphous/polycrystalline material combinations where at least one of the layers has compliant bond angles, such as in compounds with an ionic bonding character.

References and notes:

Funding: The authors acknowledge the support from NSF-DMREF grants DMR-1729779, DMR-1729016, and DMR-1842467. Computational resources were provided by NSF-MRI grant OAC-1919789.

Author contributions: WL designed and performed the overall experiment including sample preparation and analyses, XC perform sample preparations and electrical measurements, SIB and SK analyzed the HRTEM and STEM. RPHC oversaw the experiments and conceived the original multilayer structure. JM performed the theoretical calculation. WL, QS, DS, MB, VD, JBK, and JM helped prepare the manuscript, and MG led the manuscript writing. All the authors reviewed the manuscript.

Current address: WL: Department of Materials Science and Engineering, Soongsil University, 369 Sangdo-ro, Dongjak-gu, Seoul 06978, Republic of Korea

Competing interests: There are no conflicts to declare.

Accepte

This article is protected by copyright. All rights reserved.

¹ L. Esaki, R. Tsu, *IBM Journal of Research and Development*. **1970** *14*, 61.

² R. Dingle, H. L. Stormer, A. C. Gossard, W. Wiegmann, *Appl. Phys. Lett.* **1978** *33*, 665.

³ C. Waschke, H. G. Roskos, R. Schwedler, K. Leo, H. Kurz, K. Köhler, *Phys. Rev. Lett.* **1993** *70*, 3319.

⁴ J. Faist, F. Capasso, D. L. Sivco, C. Sirtori, A. L. Hutchison, A. Y. Cho, *Science* **1994** *264*, 553.

⁵ <u>A.</u> Frano, E. Benckiser, Y. Lu, M. Wu, M. Castro-Colin, M. Reehuis, A. V. Boris, E. Detemple, W. Sigle, P. van Aken, G. Cristiani, G. Logvenov, H.-U. Habermeier, P. Wochner, B. Keimer, V. Hinkov, *Advanced Materials* **2014** *26*, 258.

⁶ H. Y. Hwang, Y. Iwasa, M. Kawasaki, B. Keimer, N. Nagaosa & Y. Tokura, *Nature Materials* **2012** *11*, 103.

⁷ R. Tsu, E. H. Nicollian, A. Reisman, *Appl. Phys. Lett.* **1989** 55, 1897.

⁸ L. J. Cui, U. D. Venkateswaran, B. A. Weinstein, F. A. Chambers. *Phys Rev B* **1989** *45*, 9248.

⁹ Qiu-yi Ye, R. Tsu, E. H. Nicollian, *Phys. Rev. B* **1991** *44*, 1806.

¹⁰ Tsu, Raphael, U.S. Patent 5,216,262, **1993**.

¹¹ Seo, Yong-Jin, *Trans. Electric.l and Electronic Mat.* **2001** *2*, 16.

¹² Wang, Chia-Gee, Raphael Tsu, John Clay Lofgren. "Epitaxial SiOx barrier/insulation layer." U.S. Patent 6,376,337, **2002**.

¹³ A. Descoeudres, L. Barraud, Stefaan De Wolf, B. Strahm, D. Lachenal, C. Guérin, Z. C. Holman, F. Zicarelli, B. Demaurex, J. Seif, J. Holovsky, C. Ballif, *Appl. Phys. Lett.* **2011** *99*, 123506.

¹⁴ T.C. Chong, L.P. Shi, X.Q. Wei, R. Zhao, H.K. Lee, P. Yang, A.Y. Du, *Phys. Rev. Lett.* **2008** *100*, 136101.

¹⁵ D. J. Eaglesham, J. M. Poate, D. C. Jacobson, M. Cerullo, L. N. Pfeiffer, K. West. *Appl. Phys. Lett.* **1991** *58*, 523.

¹⁶ R. W. Fathauer, T. George, E. W. Jones, W. T. Pike, A. Ksendzov, R. P. Vasquez. *Appl. Phys. Lett.* **1992** *61*, 2350.

¹⁷ S. Miyazaki, Y. Ihara, M. Hirose, *J. Non-Cryst. Solids* **1987** *97*, 887.

¹⁸ M. Zacharias, J. Bläsing, P. Veit, L. Tsybeskov, K. Hirschman, P. M. Fauchet, *Appl. Phys. Lett.* **1999** *74*, 2614.

¹⁹ M. Zacharias, J. Bläsing, K. Hirschman, L. Tsybeskov, P. M. Fauchet. *J. Non-Cryst. Solids* **2000** 266, 640.

²⁰ Christoph Deneke, Rudeesun Songmuang, Neng Yun Jin-Phillipp, Oliver G Schmidt, *J. Phys. D: Appl. Phys.* **2009** *42*, 103001.

²¹ W.-B. Zhang, Q. Qu, K. Lai, ACS Appl. Mater. Interfaces **2017** 9, 1702.

²² M. Davide, L. Henrik, B. Arumugam Chandra, O. Kostya, *Nanotechnology* **2008** *19*, 495302.

²³ F. Ji, X. Ren, X. Zheng, Y. Liu, L. Pang, J. Jianga, S. (Frank) Liu, *Nanoscale* **2016** *8*, 8696.

²⁴ Dingle, H. L. Störmer, A. C. Gossard, W. Wiegmann, *Appl. Phys. Lett.* **1978** *33*, 665.

²⁵ K. Inoue, T. Matsuno, *Phys. Rev. B* **1993** *47*, 3771.

²⁶ T. C. L. G. Sollner, W. D. Goodhue, P. E. Tannenwald, C. D. Parker, D. D. Peck, *Appl. Phys. Lett.* **1983** *43*, 588.

²⁷ E. E. Mendez, W. I. Wang, B. Ricco, L. Esaki, *Appl. Phys. Lett.* **1985** *47*, 415.

²⁸ W. Walukiewicz, H. E. Ruda, J. Lagowski, H. C. Gatos, *Phys. Rev. B* **1984** *30*, 4571.

²⁹ M. B. Zakaria, T. Nagata, A. Matsuda, Y. Yasuhara, A. Ogura, Md. S. A. Hossain, M. Billah, Y. Yamauchi, T. Chikyow, *ACS Appl. Nano Mater.* **2018** *1*, 915.

³⁰ D. B. Buchholz, Qing Ma, Diego Alducin, Arturo Ponce, Miguel Jose-Yacaman, Rabi Khanal, Julia E. Medvedeva, Robert P. H. Chang, *Chemistry of Materials* **2014** *26*, 5401.

³¹ A. Nelson, *J. Appl. Crystallogr.* **2006** *39*, 273.

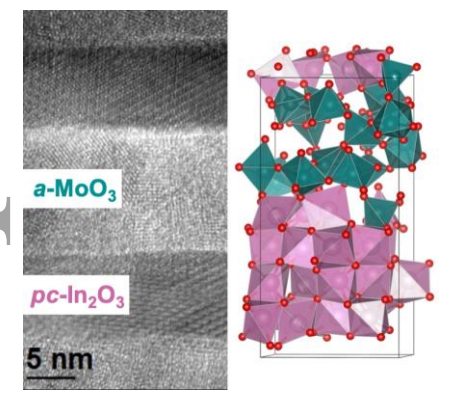
³² X.-L. Zhou, S.-H. Chen, *Physical Review E* **1993** *47*, 3174.

³³ X.-L. Zhou, *Physical Review E* **1995** *52*, 1938.

³⁴ National Institute of Standards and Technology Center for Neutron Research. http://www.ncnr.nist.gov.

³⁵ C.-C. Yu, K.-S. Yang, H. Chang, J.-S. Lee, J.-Y. Lai, P.-Y. Chuang, J.-C. A. Huang, A.-C. Sun, F.-C. Wu, H.-L. Cheng, *Vacuum* **2014** *102*, 63.

Superlattices represent the epitome of combinatorial materials science: their properties can transcend those of their constituent layers, such as improved mobility with modulation doped structures. Here superlattice combinations are expanded into the morphological domain by introducing direct growth of alternating amorphous and polycrystalline layers, realizing a high-quality, high mobility "heteromorphic superlattice," originally conceived by Raphael Tsu in 1989.



³⁶ Y. Saito, C. Kaito, T. Naiki, *J. Cryst. Growth* **1986** *79*, 436.

³⁷ A. Mazor, D. J. Srolovitz, P. S. Hagan, Bukiet, G. B, Columnar growth in thin films. *Phys. Rev. Lett.* **1988** *60*, 424.

³⁸ G. K. Williamson, W. H. Hall, X-ray line broadening from filed aluminium and wolfram. *Acta Metall.* **1953** *1*, 22

³⁹ Q. Shao, C. C. Aygen, X. Chen, W. Lee, R. P. H. Chang, J. E. Medvedeva, M. A. Grayson, unpublished.